Nanoscale

Accepted Manuscript

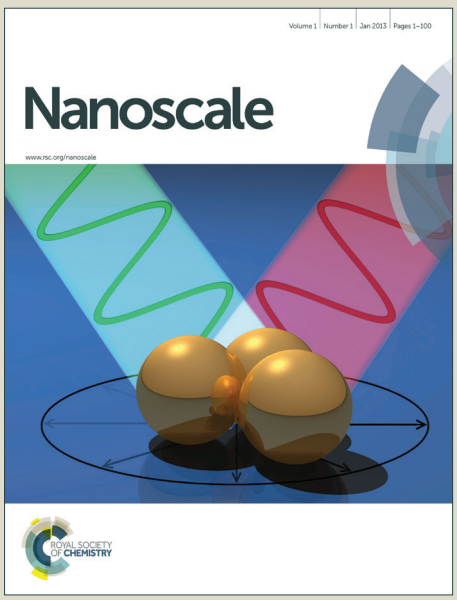

ROYAL SOCIETY OF CHEMISTRY

www.rsc.org/nanoscale

Nanoscale

PAPER

Received 00th January 20xx,

Accepted 00th January 20xx

DOI: 10.1039/x0xx00000x

www.rsc.org/

Geometrical and Morphological Optimizations of Plasmonic Nanoarrays for High-Performance SERS Detections

W. Q. Li,[a,b] G. Wang,[a,b] X. N. Zhang,[a,b] H. P. Geng,[a,b] J. L. Shen,[a,b] L. S. Wang,[a,b] J. Zhao,[a,b] L. F. Xu,[a,b] L. J. Zhang,[a,b] Y. Q. Wu,[a,b] R. Z. Tai[a,b] and G. Chen[a,b,c]

Here we present an in-depth and comprehensive study of the effect of geometry and morphology of nanoarray (NA) substrates on their surface-enhanced Raman scattering (SERS) performance. The high-quality SERS-active NA substrates of various unit shapes and pitches are assembled through electron beam lithography and fabricated by electron beam physical vapor deposition. Good agreements are found in comparing the Raman scattering results with the integrals of the fourth power of local electric fields from the three-dimensional numerical simulations. A novel type of hybrid NA substrates composed of disordered nanoparticles and a periodic NA is fabricated and characterized. The morphology of NAs has little influence on the SERS performance of hybrid NA substrates and they perform better than both their counterpart pure NA and disordered nanoparticle substrates.

Introduction

Surface-enhanced Raman scattering (SERS) has attracted a great deal of research interests since its first discovery in the 1970s[1] and become a burgeoning analytical technique for chemistry and biology. SERS-based signal and molecular sensing has been rapidly developed and widely utilized in biomedical, agricultural and environmental fields for trace detection and molecular identification, including rapid DNA sequencing[2,3] and detections of explosive,[4,5] narcotics[6,7] and pesticide.[8,9] The Raman scattering enhancement originates from localized surface plasmon resonance (LSPR) that concentrates incident light and leads to selective photon absorption and amplification of the local electromagnetic field near metal nanostructure surfaces by orders of magnitude.[10] In general, LSPR yields most mutations in locations near the sharp edges or between two adjacent metal nanostructures commonly referred to as 'hot spots'. When molecular probes reside in the hot-spot regions, their Raman scattering signal can be dramatically enhanced.[11–13]

Noble metallic nanostructures especially Ag and Au nanostructures[14] have been widely used in SERS applications, because their LSPR frequency falls into the visible range where most of the commonly-used lasers are operated. Metallic SERS substrates of various geometries and morphologies have been prepared by numerous assembling methods with the ultimate detection capability achieved at single-molecule level by optimizing their sizes, shapes, compositions, inter-gap distances and dielectric environments.[15–18] Over the years, in addition to simple nanostructures such as nanospheres,[19] nanorods,[20,21] and nanowires,[22] many unique composite nanostructures have been fabricated, for example, Au-coated Si nanopillar arrays,[23] Ag-SiO_2 core-shell nanocubes,[24] and Au-decorated flowerlike ZnO/Si arrays.[25] It has been demonstrated that nanoparticles present in either aggregated forms or as arrays generate greater SERS signal because of the coupling of electromagnetic fields between adjacent nanoparticles leading to very strong fields in the interstitial regions.[26,27] As a result, preparing effective noble metallic nanostructures as SERS-active substrates has recently attracted a lot of attentions.[28-30] Three-dimensional nanoarrays (NA) have the advantage of large surface areas available for target analytes to attach. In addition, theoretical models indicate that periodic NAs could exhibit higher SERS efficiency as compared to randomly arranged nanostructures, because the retardation or damping effects are less critical to the electromagnetic field enhancement of periodic NAs.[31]

With the development of nanotechnology, effective, repetitive, stable and environment-friendly SERS-active substrates have been assembled through chemical syntheses and nanofabrications. Conventional methods such as solution-phase syntheses including polyol process[32–34] and seed-mediated growth[35,36] are simple and popular ways to generate noble metal nanostructures, but they are hard to control the uniformity of the final products. Meanwhile, template-based techniques including anodized aluminium and nanosphere lithography[37–39] are able to prepare nanostructures with well-defined sizes and shapes under the assistance of templates, but they are limited by accessible structures and challenged by

[a] Shanghai Synchrotron Radiation Facility, Shanghai Institute of Applied Physics, Chinese Academy of Sciences, Shanghai 201204, China. E-mail: tairenzhong@sinap.ac.cn.
[b] CAS Key Laboratory of Interfacial Physics and Technology, Shanghai Institute of Applied Physics, Chinese Academy of Sciences, Shanghai 201204, China.
[c] School of Physical Science and Technology, ShanghaiTech University, Shanghai 201210, China. E-mail: gchen@shanghaitech.edu.cn.

creating nanostructures with small unit sizes and inter-gaps. In this regard, electron beam lithography (EBL) capable of fabricating NAs with not only controllable and reproducible sizes and shapes but also excellent uniformity provides compelling route to prepare high-quality SERS substrates. With the assistant of a microfocus Raman setup, substrates prepared with EBL are amenable to practical SERS applications.

Herein, we applied EBL and E-beam evaporation techniques in fabricating noble metal NAs as SERS-active substrates. The effect of the NA morphology and geometry on its SERS performance was systematically studied on a series of substrates with various nanoparticle (NP) shapes and inter-particle distances. The spatial distributions of the electromagnetic field of the NA substrates were simulated by finite-difference time-domain (FDTD) method. Qualitative comparisons between the numerical results and the experimental data were carried out by taking the total local electric field enhancement around a single NP unit. A novel type of hybrid NA substrates composed of disordered NPs and a periodic NA was fabricated and characterized. This new type of substrates was able to surpass some technical barriers of EBL and gain better SERS performance than its pure NA counterpart.

Experimental Section

Au nanoarray SERS-active substrate fabrication

Substrate-supported Au nanoarrays were fabricated by electron beam lithography (EBL, CABL-9500C). A 80-nm poly(methyl methacrylate) (A2 PMMA, 950K molecular weight) resist was spin-coated at 4000 rpm onto a pre-cleaned Si substrate, then baked at 180 °C for 90 s, and followed by the electron beam exposure. The exposed PMMA was then developed in a 3:1 developer solution of IPA:MIBK for 45 s and cleaned by the ethanol and deionized water. Finally, 2-nm of Cr adhesion layer and 20-nm thick Au film were evaporated successively onto the substrate. Following lift-off of the PMMA resist by sonicating the samples in acetone, the area (120 ×120 μm^2) of Au nanoarrays remained. The Au film covered nanoarray substrate was formed by evaporating a 15-nm Au film onto the pure Au nanoarray substrate. In order to add disordered Au NPs onto the Au nanoarray substrate, a 10-nm Au film was evaporated onto the substrate at 200 °C and then annealed in vacuum.

Optical measurements

The structure of the fabricated Au nanoarrays was examined by field-emission scanning electron microscope. SERS spectra were acquired using a fiber-optic coupled, confocal Raman microscope with a CCD-equipped spectrograph (XploRA INV). A fiber-optic interfaced 638-nm wavelength diode laser was used to provide the incoming radiation at room temperature from the topside of samples. The focused spot size was about 1 μm. The samples were prepared by dropping 10^{-4} M p-Nitrobenzenethiol (PNBT) solution onto SERS-active substrates and left until natural dry before Raman measurements. The reflective spectra were acquired using a micro-photospectrometer with a spectrometer coupled to an optical microscope.

Numerical modeling

To model the optical properties of Au nanoarray substrates, we use the finite-difference time-domain method to calculate near-field intensity $|E|^2$ enhancements of the nanostructures. Nine Au NP units were used in the FDTD calculations to simulate the nanoarrays used in the experiments. A plane wave light source polarized along the x-axis with its wavelengths ranging from 400 to 800 nm was used in numerical simulations. The dielectric constant of Au was selected from the material database of the Lumerical FDTD solutions and the background relative dielectric constant was assumed to be 1. A three-dimensional monitor was placed parallel to the substrate and covered the whole nanostructure in order to acquire the full map of the electric fields.

Results and discussion

Geometrical and morphological characterization of SERS-active NA substrate

The SERS-active NAs were prepared through E-beam evaporation of Au substance onto Si substrate supported templates fabricated by EBL. A schematic diagram of the sample preparation procedure is shown in Fig 1. First, PMMA resist was spin-coated onto a pre-cleaned Si substrate before electron beam exposure. Next, the exposed PMMA was processed in a developing solution of IPA:MIBK. Finally, a 2-nm Cr adhesion layer and a 20-nm Au film were evaporated successively onto the PMMA template. Following the lift-off of PMMA resist by sonicating the samples in acetone, the fabricated area (120 ×120 μm^2) of Au NAs remained. For all the samples, the height of Au NAs was kept at 20 nm.

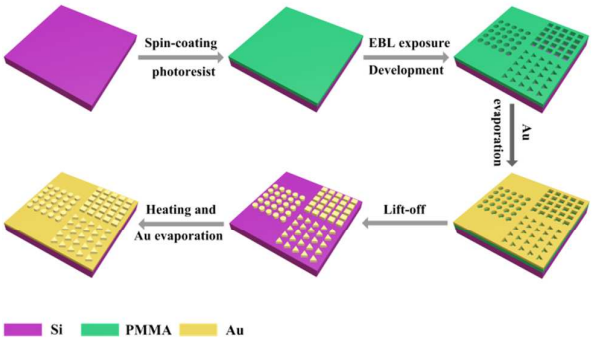

Fig 1. A schematic diagram of the fabrication process of nanoarray substrates.

As shown by their SEM images in Fig 2, the circular, square and triangular Au NAs were fabricated with their unit NP size of 100 nm and inter-gaps of 30, 50, 70 and 100 nm, respectively. It is noteworthy that the NAs prepared by EBL are

highly uniform and ordered. For Au NA substrates, aromatic thiol molecules are one of the most popularly used probes due to the strong and stable Au–S bonding and the large scattering cross section of benzene rings.[40] On this account and also due to its well established vibrational features in Raman spectra, PNBT known as the intermediate product of organic pollutants presenting in medicine, pesticides and dyestuff was chosen as the probe molecule in this work. The intense peaks at 1076,

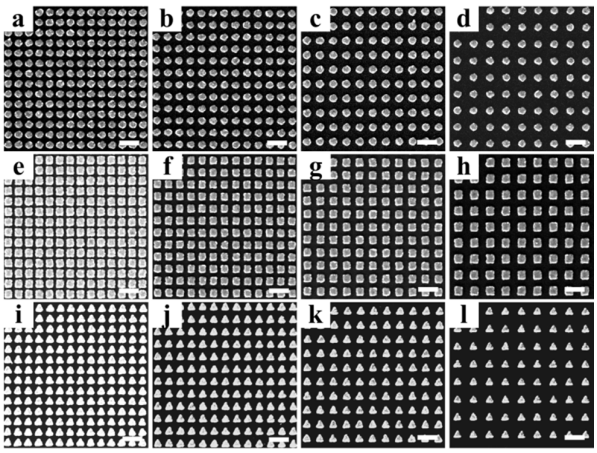

Fig 2. SEM images of different inter-gaps (from left to right panels, the inter-gaps are 30, 50, 70 and 100 nm, respectively) of circular, square and triangular nanoarrays with a fixed unit size of 100 nm deposited on Si substrates. The scale bars in the figures are 300 nm.

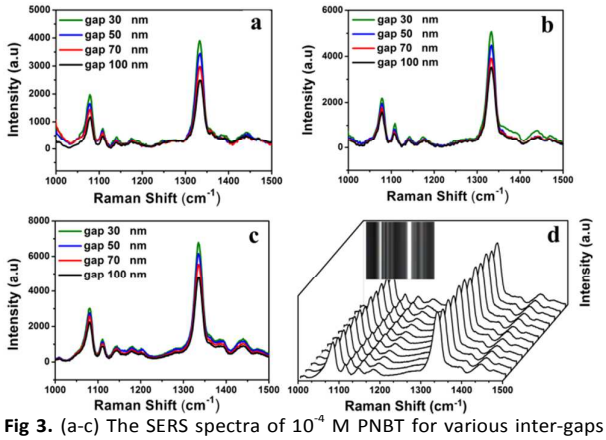

Fig 3. (a-c) The SERS spectra of 10^{-4} M PNBT for various inter-gaps of circular, square and triangular nanoarray substrates with the fixed 100 nm unit size. (d) The SERS spectra of 10^{-4} M PNBT measured at 12 randomly selected spots on the square nanoarray substrate with its unit size of 100 nm and inter-gap of 30 nm. The inset is the Raman intensity mapping.

1108, 1140, 1177, 1333 and 1442 cm^{-1} are the main vibrational modes of PNBT molecules. As shown in Fig 3a-c, for NAs with the same NP shape and size, their SERS intensity increases as the inter-gap decreases. As previously reported,[41] a large inter-gap results in weak electric field coupling between neighboring NPs and hence low Raman intensity from the molecules in between. As shown in Fig 3d, the SERS signals from 12 randomly selected spots on the 30-nm inter-gap square NA substrate were measured with a walking step of 6 μm. The SERS spectra nearly overlap indicating the NA substrate is highly uniform with the relative standard deviation (RSD) of the peak intensity at 1333 cm^{-1} being 6.4%. The Raman spectroscopic mapping shown in the inset also manifests the substrate is very homogeneous. This is crucial for practical SERS applications, because the laser spots of Raman spectrometers generally cover a micron-meter size spot and the preparation of periodic and uniform substrates at this scale ensures reproducible and consistent results.

Numerical simulations were performed with FDTD to analysis the electric field distributions of the NA substrates upon the irradiation of 638-nm wavelength light. In order to acquire the full electric field distribution around a NP, we created a three-dimensional (3D) monitor by putting multiple two-dimensional recorders along the direction normal to a substrate during FDTD simulations (details see Experimental Section). The 3D electric field distribution profile of the circular

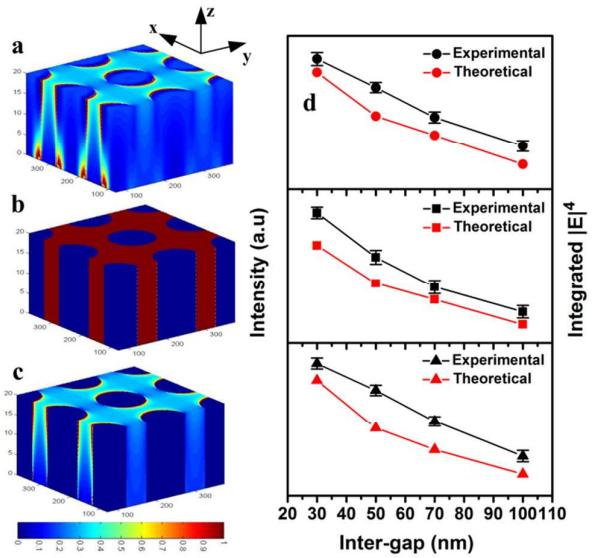

Fig 4. (a) The three-dimensional electromagnetic field map of the circular nanoarray on a Si substrate. (b) A filter for the circular nanoarray. (c) The electromagnetic field map after filtrating the fields inside the nanoparticles. (d) The integrated SERS peak intensity at 1333 cm^{-1} and the fourth power of the theoretical integrated electromagnetic field $|E|^4$ as a function of the inter-gap for circular, square and triangular nanoarray substrates (from top to bottom, the symbols represent the shape of the nanoarray units). The error bars in the experimental data are standard deviation of SERS peak intensity at 1333 cm^{-1}.

NA is shown in Fig 4a. Since Raman scattering enhancement scales with the fourth power of local electric fields $|E|^4$,[42,43] enormous signal enhancements have been reported for metallic nanostructures.[44,45] In view that the electric field is not uniformly distributed around a NP,[46] we calculate the total

intensity of $|E|^4$ by integrating it in the whole space,[41] $I_u = \int |E|^4 dv$. Because the probe molecules could only absorb on the outer surfaces (top and side) of NPs, the $|E|^4$ inside is subtracted from the total integral of $|E|^4$ by applying a filter shown in Fig 4b, leaving the fields outside alone to be integrated (Fig 4c). As shown by the results in Table 1, the electric fields mainly distribute in the outer space and the intensities inside the NPs are relatively weaker but appreciable for all the samples. For NAs with the same unit morphology, the particle densities vary in the same spot covered by a laser beam due to the difference in their inter-gaps. In order to compare their SERS performance, the integrated $|E|^4$ values in a laser spot (I_t) are normalized by the particle density, $I'_t = (I'_u/I_u) \cdot (s_u/s'_u) \cdot I_t$, where s_u is the area covered by a NP unit. In Fig 4d, the integrated scattering peak intensities at 1333 cm^{-1} are plotted as a function of the inter-gap for NA substrates with different unit shapes. They are in good agreement with the integrations of $|E|^4$ calculated by FDTD. These studies show the SERS signal increases with decreasing inter-gap distances for NAs with the same unit NP size and morphology.[47,48]

Table 1 The integrated intensity $|E|^4$of different position of NP with various shape at 638 nm

	total	inside	outside
circlular	5.37E+04	2.25E+04	3.12E+04
square	5.28E+04	1.71E+04	3.57E+04
triangular	7.43E+04	2.56E+04	4.87E+04

The influence of morphology on the SERS performance of NA substrates is also delineated in this section. As shown in Fig

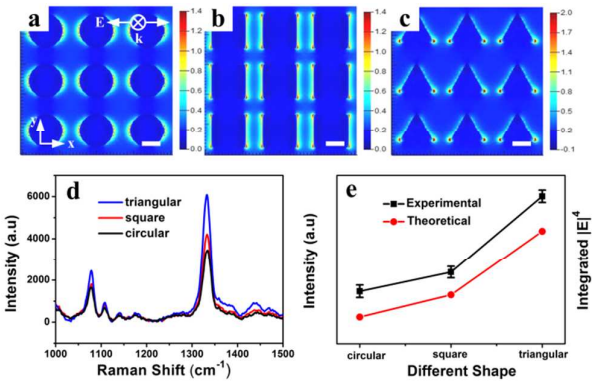

Fig 5. (a-c) Electric field maps of circular, square and triangular nanoarrays of 100 nm size and 50 nm inter-gap on Si substrates. The scale bars in figures are 50 nm. (d) The SERS spectra of PNBT for different unit shapes of nanoarray substrates. (e) The integrated SERS peak intensity at 1333 cm^{-1} and the fourth power of the theoretical integrated electromagnetic field $|E|^4$ as a function of the nanoarray unit shape. The error bars in the experimental data are the standard deviations of the SERS peak intensities at 1333 cm^{-1}.

5a-c, the electric field distributions are simulated by FDTD for the circular, square and triangular Au NAs with the NP size of 100 nm and the inter-gap of 50 nm. As can be seen, the electric fields are mainly distributed around the NP edges. For triangular and square NAs, the strongest electric fields are observed around their NP tips where the probe molecules would emit the strongest Raman scattering signal. As shown in Fig 5d, the triangular NA exhibits the strongest SERS intensity while the circular one shows the weakest, illustrating the significant effect of NP morphology on the SERS performance of NA substrates. The integrated scattering peak intensities at 1333 cm^{-1} are plotted as a function of the unit shape of NAs. The integral of the fourth power of electric field $|E|^4$ is calculated using the procedure shown in Fig 4a-c. As shown in Fig 5e, it shows the same trend as the SERS intensities measured experimentally.

Geometrical and morphological characterization of SERS-active hybrid NA substrates

A novel type of SERS-active hybrid NA substrates, composed of disordered NPs and periodic NAs, was formed by annealing (200 °C) the 10-nm Au thin film covered NA substrates in vacuum (details see Experimental Section). The SEM profiles of the hybrid NA substrates with different matrix unit shapes (circular, square and triangular) and inter-gaps (30, 50, 70 and

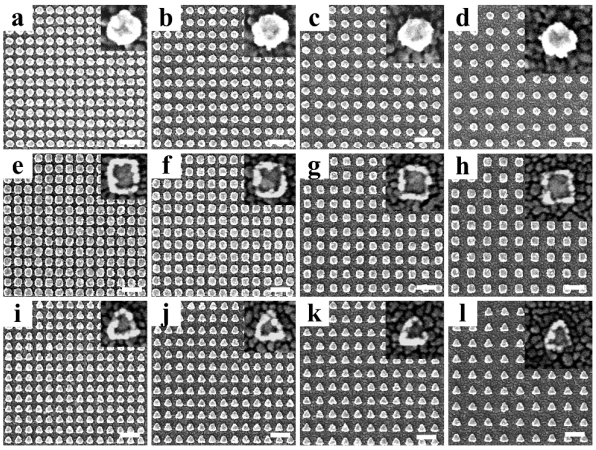

Fig 6. SEM images of different inter-gaps (from left to right panels, the inter-gaps are 30, 50, 70 and 100 nm, respectively) of circular, square and triangular nanoarrays with a fixed unit size of 100 nm covered by disordered nanoparticles on Si substrates. The scale bars in the figures are 300 nm. The insets are the high-magnification SEM images of the hybrid NA substrate units.

100 nm) are shown in Fig 6. As can be seen, the disordered NPs are distributed on the side and top of the periodic NAs. The SERS performance of the hybrid NA substrates with different unit shapes and inter-gap distances is shown in Fig 7a-c. The Raman signal decreases with increasing inter-gap distances regardless of the NA unit shape. Fig 7d shows the SERS signals from PNBT molecules for 12 randomly selected

spots on the 30-nm inter-gap hybrid square NA substrate measured at a walking step of 6 μm. The SERS spectra along with the Raman spectroscopic mapping in the inset demonstrate the uniformity of hybrid NA substrates. While the hybrid NA substrate has a larger RSD value of 15.4% for SERS signals than its pure NA counterpart (6.4%), it is well within the tolerance for practical applications (20%).[49]

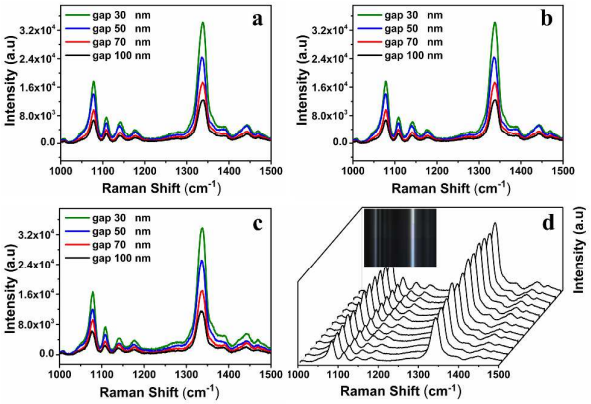

Fig 7. (a-c) The SERS spectra of 10^{-4} M PNBT for various inter-gaps of circular, square and triangular hybrid nanoarray substrates with the fixed 100 nm unit size. (d) The SERS spectra of 10^{-4} M PNBT measured at 12 randomly selected spots on the square hybrid nanoarray substrate with its unit size of 100 nm and inter-gap of 30 nm. The inset is the Raman intensity mapping.

The influence of the NA unit morphology on the overall SERS performance of hybrid NA substrates is evaluated on three substrates with circular, square and triangular NAs and having the same unit size of 100 nm and inter-gap of 50 nm. From the SERS spectra shown in Fig 8a, we find that the Raman signals from the hybrid NA substrates are improved significantly compared to the ones on bare Si substrates while the NP shape has nearly no influence on their overall intensities. In Fig 8b, we compare the SERS spectra from the ordered triangular NA, the annealed Au film and the hybrid NA substrate with disordered Au NPs around a triangular NA. The SEM image of the disordered Au NPs on a bare Si substrate is shown in the inset. By integrating the areas under the Raman scattering peaks at 1333 cm^{-1}, we found the Raman signal for the hybrid NA substrate is 1.6 times that of the disordered NP substrate and 4 times that of the ordered NA substrate under the same experimental conditions. These results clearly indicate that the disordered Au NPs play a prominent role in regulating the plasmonic modes of hybrid NA substrates.

In order to evaluate the effect of disordered Au NPs on the SERS performance of NA substrates, we measure a large number of individual NPs from their SEM images and obtain the statistical distributions of their diameters and inter-gap distances. As shown in the insets of Fig 8c and d, the NA substrates are covered by small disordered NP islands with their sizes mainly in the range of 5～50 nm and inter-gaps of 1～11 nm. As shown in Fig 8c, the integrated $|E|^4$ values are obtained from FDTD simulations by keeping the NP diameter at its statistical mean value (20 nm) and plotted as a function of inter-gap distances. As can be seen, the integrated $|E|^4$ increases linearly as the inter-gap distance decreases from 11 to 3 nm, but it rises rapidly for inter-gap distances smaller than 3 nm and reaches its maximum at 1 nm. Beyond 1 nm, the values decrease dramatically but as been previously pointed out,[50] FDTD simulations may no longer be valid in this region. In Fig 8d, the integrals of $|E|^4$ are calculated as a function of

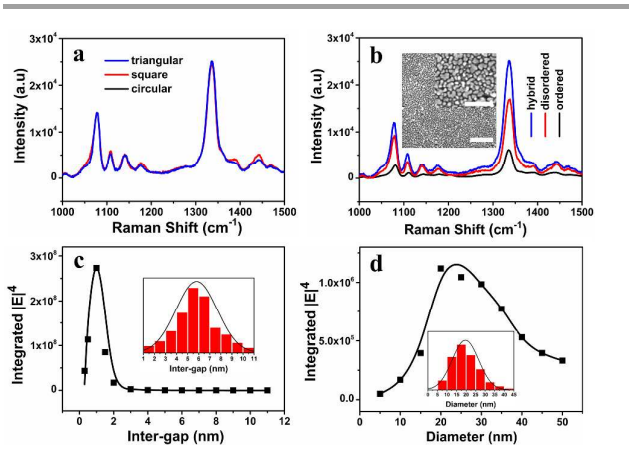

Fig 8. (a) SERS spectra of 10^{-4} M PNBT for hybrid nanoarray substrates of different unit shapes with the fixed size of 100 nm and inter-gap of 50 nm. (b) Comparison of the SERS performance of the triangular nanoarray, disordered nanoparticle and hybrid triangular nanoarray substrates. The inset are the SEM images of disordered nanoparticles on a Si substrate under different magnifications. The scale bars in the figure are 300 nm. (c-d) The theoretical integrated electric field $|E|^4$ is plotted as a function of the inter-gap and diameter of disordered nanoparticles (the insets are the statistic inter-gap distance and size distributions of the disordered nanoparticles).

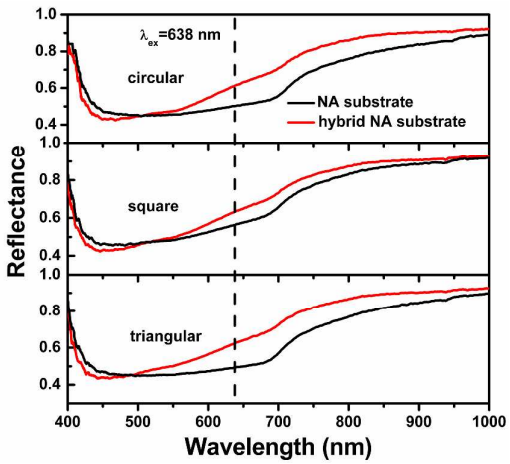

Fig 9. Comparison of the reflective spectra of nanoarray and hybrid nanoarray substrates with the 100-nm circular, square and triangular unit sizes and the 50-nm inter-gaps. The dashed line denotes the laser excitation wavelength.

NP diameters with the inter-gap distance kept at its statistical mean value (6 nm). In this case, the integrated $|E|^4$ has a maximum value for the NP diameter at around 23 nm and decreases monotonically on both sides of it. Since SERS signals are linearly proportional to the integrated $|E|^4$ values, the plots in Fig 8c and d can reflect the SERS performance of the corresponding NA substrates. As can be seen from Fig 6a-l and the inset of Fig 8b, for the annealed Au films, most of the inter-gaps between the disordered NPs are smaller than 10 nm. For NA substrates with the same NP size, SERS signals increase with decreasing inter-gap distances, but it is normally difficult to use EBL method to fabricate NAs with inter-gaps less than 10 nm. In this regard, the annealed Au films provide desirable inter-gaps for SERS-active NA substrates. Moreover, their NP size distribution is also favorable for SERS performance as its mean value is close to the peak position of the curve shown in Fig 8d. For hybrid NA substrates, SERS enhancement originates from the electromagnetic coupling between the ordered and disordered NPs in addition to the ones among themselves. Compared to pure NA substrates, hybrid NA substrates induce two extra terms of electromagnetic interactions and consequently generate more 'hot spots'. As shown in Fig 8b, the hybrid NA substrate produces stronger SERS intensity than both its counterpart pure NA and disordered NP substrates. The periodic NA may play a role in hybrid NA substrates by reducing the retardation and damping of the electromagnetic field caused by the disordered NPs and consequently improves its SERS performance.[31,51] The UV-visible reflective spectra of the NA and hybrid NA substrates with the 100-nm circular, square and triangular unit sizes and the 50-nm inter-gaps are shown in Fig 9. A strong and broaden reflectivity dip centered around 460 nm is assigned to the absorption of Au plasmon.[52]

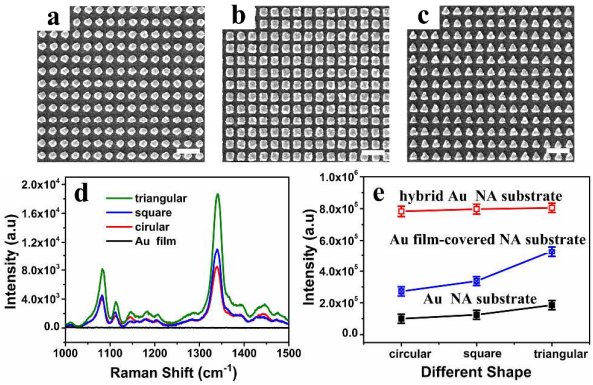

Fig 10. SEM images of (a) circular, (b) triangular, and (c) square Au nanoarray substrates with their unit size of 100 nm and inter-gap of 50 nm covered by 15-nm thick Au films. The scale bars in the figures are 300 nm. (d) SERS spectra of 10^{-4} M PNBT for different unit shapes of Au film covered nanoarray substrates along with the Au film substrate. (e) Comparison of the experimental Raman scattering peak intensities at 1333 cm^{-1} for three types of SERS-active substrates with the same unit size of 100 nm and inter-gap of 50 nm. The error bars in the figure are the standard deviations of SERS peak intensity at 1333 cm^{-1}.

As a comparison, Au film-covered NA substrates were prepared by depositing 15-nm Au films without further annealing. Fig 10a-c show the SEM images of the Au film-covered NA substrates with circular, triangular and square unit NPs. As shown in Fig 10d, there is no observable Raman scattering feature from the flat Au film substrate without NAs, but strong signals are collected on the Au film-covered NA substrates. The influence of NP morphologies on the SERS performance of Au film-covered NA substrates has the same trend as that for bare Si substrates. The SERS responses of three types of NA substrates, each with three different kinds of unit NP shapes, are compared in Fig 10e. The hybrid NA substrates have the strongest Raman signals than both Au film-covered and pure Au NA substrates. Meanwhile, the SERS signals for PNBT on Au film-covered NA substrates are comparably stronger than bare Si substrates, which is related to the dielectric constants of substrates.[53]

Conclusions

In this work, a series of SERS-active NA substrates with circular, triangular and square NP units and various inter-gaps are prepared using EBL method. Their SERS performance is comprehensively evaluated through Raman scattering experiments and FDTD simulations. Under the same conditions, the triangular NA substrate and the substrates with small inter-gaps have high SERS enhancement factors. These studies clearly point to the direction for making high-performance NA substrates, nevertheless it is technically challenging for EBL to fabricate NAs with inter-gaps smaller than 10 nm. By thermal annealing of the Au film covered NA substrates, NP islands were formed with not only small inter-gaps but also adequate statistical size distribution for high SERS performance. The hybrid NA substrate benefits from both of these constructive factors of the disordered NPs and the periodicity of NAs that could mitigate the electromagnetic field retardation effect, and hence scores a higher SERS enhancement factor and gains better detection sensitivity than both its counterpart pure NA and disordered NP substrates. Moreover, its uniformity and SERS signal reproducibility are also good to meet the criterions for practical applications. The simplicity in fabrication and merit in performance make the hybrid NA substrates ideal for use in SERS-based sensing and characterizations of chemical and biological molecule structures.

Acknowledgements

This study was supported by Open Research Project of Large Scientific Facility from Chinese Academy of Sciences: Study on Self-assembly Technology and Nanometer Array with Ultra-high Density. G.C. acknowledges the support from the National Natural Science Foundation of China (11375256) and Science and Technology Commission of Shanghai Municipality

(14JC1493300). R.Z.T. acknowledges the support from the Shanghai Academic Leadership Program (13XD1404400) and the National Natural Science Foundation for Outstanding Young Scientists (11225527). We thank all the team members at BL08U of Shanghai Synchrotron Radiation Facilities (SSRF) for sample preparation.

Notes and references

1 M. Fleischman, P. J. Hendra, A. J. Mcquillan, *Chem. Phys. Lett.*, 1974, **26**, 163.
2 S. J. Park , T. A. Taton , C. A. Mirkin, *Science*, 2002, **295**, 1503.
3 L. A. Gearheart, H. J. Ploehn, C. J. Murphy, *J. Phys. Chem. B*, 2001, **105**, 12609.
4 J. M. Sylvia, J. A. Janni, J. D. Klein, K. M. Spencer, *Anal. Chem.*, 2000, **72**, 5834.
5 L. Yang, L. Ma, G. Chen, J. Liu, Z-Q Tian, *Chemistry*, 2010, **16**, 12683.
6 J. C. Carter, W. E. Brewer, S. M. Angel, *Appl. Spectrosc.*, 2000, **54**, 1876.
7 S. E. Bell, N. M. Sirimuthu, *Analyst*, 2004, **129**, 1032.
8 X. Han, H. Wang, X. Ou, X. Zhang, *J. Mater. Chem.*, 2012, **22**, 14127.
9 J. F. Li, Y. F. Huang, Y. Dingetal, *Nature*, 2010, **464**, 392.
10 J. Theiss, P. Pavaskar, P. M. Echternach, R. E. Muller, S. B. Cronin, *Nano Lett.*, 2010, **10**, 2749.
11 H. Xu, J. Aizpurua, M. Kall, P. Apell, *Phys. Rev. E.*, 2000, **62**, 4318.
12 M. Moskovits, *J. Raman Spectrosc.*, 2005, **36**, 485.
13 Z. Li, T. Shegai, G. Haran, H. Xu, *ACS Nano.*, 2009, **3**, 637.
14 A. Ramón, Alvarez-Puebla, M. Luis, Liz-Marzán, *Small*, 2010, **6**, 604.
15 R. A. Álvarez-Puebla, *J. Phys. Chem. Lett.*, 2012, **3**, 857.
16 J. Zhang, S. Li, J. Wu, G. C. Schatz, C. A. Mirkin *Angew. Chem. Int. Ed.*, 2009, **48**, 7787.
17 J. N. Anker, W. P. Hall, O. Lyandres, J. Zhao, R. P. Van Duyne, *Nat. Mater.*, 2008, **7**, 442.
18 H. Ko, S. Singamaneni, V. V. Tsukruk, *Small*, 2008, **10**, 1576.
19 M. Rycenga, M. H. Kim, C. Cobley, Y. Xia, J. *Phys. Chem. A*., 2009, **113**, 3932.
20 J. D. Driskell, S. Shanmukh, Y. J. Liu, *J. Phys. Chem. C*, 2008, **112**, 895.
21 G. Laurent, N. Félidj, J. Aubard, G. Lévi, *J. Chem. Phys*., 2005, **122**, 011102.
22 G. Sauer, G. Brehm, S. Schneider, H. Graener, *J. Appl. Phys*., 2005, **97**, 024308.
23 A. Shevchenko, V. Ovchinnikov, A. Shevchenko, *Appl. Phys. Lett.*, 2012, **100**, 171913.
24 M. Rycenga, X. Xia, C. H. Moran, Y. Xia, *Angew. Chem. Int. Ed*., 2011, **50**, 5473.
25 Y. F. Chan, H. J. Xu, L.Cao, Y. Tang, *J. Appl. Phys*., 2012, **111**, 033104.
26 F. J. GarciaVidal, J. B. Pendry, *Phys. ReV. Lett*., 1996, **77**, 1163.
27 S. L. Zou, G. C. Schatz, *Chem. Phys. Lett*., 2005, **403**, 62.
28 Z. Q. Tian, B. Ren, D. Y. Wu, *J. Phys. Chem. B*, 2002, **106**, 9463.
29 A. Gopinath, S. V. Boriskina, N. N. Feng, B. M. Reinhard, L. D. Negro, *Nano Lett.,* 2008, **8**, 2423.
30 A. Gopinath, S. V. Boriskina, W. R. Premasiri, L. Ziegler, B. M. Reinhard, L. D. Negro, *Nano Lett.,* 2009, **9**, 3822.
31 D. A. Genov, A. K. Sarychev, V. M. Shalaev, A. Wei, *Nano Lett*, 2004, **4**, 153.
32 M. Rycenga, C. M. Cobley, J. Zeng, *Chem. Rev.*, 2011, **111**, 3669.
33 Y. Xia, Y. Xiong, B. Lim, S. E. Skrabalak, *Angew. Chem. Int. Ed.*, 2009, **48**, 60.
34 A. R. Tao, S. Habas, P. Yang, *Small*, 2008, **4**, 310.
35 Q. Zhang, W. Li, C. Moran, *J. Am. Chem. Soc.*, 2010, **132**, 11372.
36 J. Zeng, X. Xia, M. Rycenga, P. Henneghan, Q. Li, Y. Xia, *Angew. Chem. Int. Ed.*, 2011, **50**, 244.
37 J. Wang, L. Huang, L. Yuan, *Appl. Surf. Sci.*, 2012, **258**, 3519.
38 S. Yang , Y. Lei, *Nanoscale*, 2011, **3**, 2768.
39 W. Zhang, X. Qiao, J. Chen, *Mater. Sci. Eng. B*, 2007, **142**, 1.
40 L. M. Tong, T. Zhu Z. F. Liu. *Chem. Soc. Rev.*, 2011, **40**, 1296.
41 Y. J. Liu, Z. Y. Zhang, Q. Zhao, Y. P. Zhao, *Appl. Phys. Lett.*, 2008, **93**, 173106.
42 E. C. Le Ru, P. G. Etchegoin, *Chem. Phys. Lett.*, 2006, **423**, 63.
43 B. Fazio, *ACS Nano*, 2011, **5**, 5945.
44 E. C. Le Ru, *J. Phys. Chem. C*, 2008, **112**, 8117.
45 S. Lal, N. K. Grady, G. P. Goodrich, N. J. Halas, *Nano Lett.*, 2006, **6**, 2338.
46 E. C. Le Ru, P. G. Etchegoin, *J. Chem. Phys.*, 2009, **130**, 181101.
47 E. Hao, G. C. Schatz, *J. Chem. Phys.*, 2004, **120**, 357.
48 Z. L. Yang, Q. H. Li, B. Ren, Z. Q. Tian, *Chem. Commun.*, 2011, **47**, 3909.
49 M. J. Natan, *Faraday Discuss.*, 2006, **132**, 321.
50 K. J. Savage, M. M. Hawkeye, J. J. Baumberg, *Nature*, 2012, **491**, 574.
51 Z. B. Wang, B. S. Luk'yanchuk, D. J. Whitehead, Z. Liu, K. G. Watkins, *J. Chem. Phys.,* 2008, **128**, 094705.
52 D. C. Rodrigues, G. F. S. Andrade, M. L. A. Temperini, *Phys. Chem. Chem. Phys.,* 2013, **15**, 1169.
53 T. Wang, Z. S. Zhang, M. W. Shao, *Sci. Rep.*, 2014, **4**, 4052.